Modelling Simul. Mater. Sci. Eng. 2 (1994) 1153–1170. Printed in the UK

Simulation of dynamic fracture of an impact-loaded brittle solid

R W Smith† and D J Srolovitz†‡

† Department of Materials Science and Engineering, The University of Michigan, Ann Arbor, MI 48109, USA

‡ Department of Materials and Interfaces, Weizmann Institute of Science, Rehovot 76100, Israel

Received 1 March 1994, accepted for publication 30 May 1994

Abstract. A new model for simulating dynamic fracture in impact-loaded solids is presented. This model is based upon the traditional molecular dynamics procedure, but accounts for the irreversible nature of the fracture process by deleting the attractive part of the particle interaction potential when the bond between two particles is stretched beyond a critical length. This critical length is determined by comparison with Griffith theory. In the present paper, the model is applied to a two-dimensional homogeneous solid in the absence of microstructure (microstructural effects are treated in a subsequent publication). When the impact zone is much smaller than the size of the sample, or the impact zone is wide and the impact amplitude is large, the first crack forms a finite distance ahead of the impact zone. Static continuum elasticity theory shows that the position of this first crack occurs at the position of the maximum tensile stress. This crack then propagates back to the edges of the impact zone and forward into the sample, thereby creating an X-shaped crack pattern. The tips of the X-shaped crack propagate more slowly than the stress wave and hence strong deviations from this pattern are observed when the stress wave passes the crack tips. When the predominantly compressive stress wave reflects off the back free surface, a tensile wave propagates back into the sample creating even more damage. This damage occurs in bands parallel to and set back from the back surface.

1. Introduction

The effects of impact loading of materials is critical for a wide range of applications. In most applications, impact resistance is not the most critical material property, but rather it is just one of many material properties that needs to be included in the optimization of a material for a particular application. However, in other applications, such as in armor, impact resistance is of pre-eminent importance. In either case, it is important to understand the relationship between material composition and microstructure and the resultant impact behavior of the material.

While the response of metals to high-rate deformation and impact has been actively studied for the past half century, the response of brittle, ceramic materials to these types of loading conditions has only recently become an area of intense research [1]. The responses of metals and ceramics to high loading rates are quite different owing to the inherent brittleness/low ductility and high moduli of ceramics, as compared with metals. Recent studies [2–4] have shown that fracture of ceramics, such as alumina (Al_2O_3), under high-rate loading, can typically occur below the Hugoniot elastic limit. The observation [3] of a transition from intergranular to transgranular fracture with increasing strain rate points to the important interplay between microstructure and fracture in impact loading. Louro *et al*

0965-0393/94/061153+18$19.50

[4] further demonstrated this link by showing that the fracture of alumina, in a series of flier plate (stress pulse) experiments, was nucleated at internal defects (voids) within the material.

Several computer simulation methods have been applied to the problem of predicting the effects of impact loading of materials. One common approach, is the use of hydrocodes (see [5] for an Eulerian hydrocode application to impact). This approach has proven to be successful in applications to metals. However, most applications of this technique contain no information about the microstructure of the material. High-rate deformation has also been examined using the finite element method (FEM) [6]. As with the hydrocodes, FEM approaches typically do not account for the effects of microstructure. It is, however, possible to include microstructure and its effects on fracture using these approaches. Unfortunately, doing so is not computationally practical because of the fine level of discretization and the frequent remeshing that would be required.

Several authors (e.g., [7–10]) have applied atomistic simulation methods to predict the properties of materials under impact loading conditions. In these studies, the material and the projectile are modeled as a small number of atomic planes and small atomic clusters, respectively. These simulations employed the classical molecular dynamics (MD) method and Lennard-Jones potentials to simulate both material and projectile. Holian [7] showed that MD simulations could capture many of the physical characteristics of an experimental study of a lead projectile impacting a thin lead plate. Although in ceramic materials, fracture and fragmentation would be expected, no fracture was observed in either simulation or experiment, owing to the high ductility of lead. In fact, MD simulations at very low temperature show no fragmentation at all. In a later study, Holian *et al* [8] applied both pairwise and embedded atom method (EAM) potentials [9] to the study of a disk impacting a wall (in two dimensions) at low temperature. While both simulations displayed ductile behavior, the simulations employing the EAM potential produced significantly more plastic flow. At high temperatures, however, simulations of both expanding liquid clusters [11, 12] and impact loaded solids [10] show that fragmentation may be nucleated by thermal fluctuation. While interesting, we believe such thermal fluctuation induced fragmentation results are inapplicable to 'real' materials, since 'real' materials always have microstructure and defects which serve as the predominant nucleation sites for cracks. Nonetheless, atomistic simulation based upon the MD method has an important advantage over continuum treatments: namely, the fact that it need only be parametrized at the atomic level, with no need to put in *ad hoc* assumptions regarding the deformation properties of the material.

In the present study, we extend the molecular dynamics technique in order to make it applicable to materials which tend to fail in a brittle manner, by fragmentation. The model itself is constructed as a two-dimensional spring-mass network in which each particle represents many atoms. The springs behave in accordance with an appropriate interparticle potential. Apart from the geometry of the lattice, all of the relevant physics is imparted into the potentials. In particular, we fit the potentials to the static properties of alumina and examine both particle and flier-plate types of impact loading in a two-dimensional brittle solid. In the next section, we describe the MD simulation approach. We then apply this MD simulation method to the fracture and fragmentation of a brittle solid without microstructure. Section 4 provides an interpretation of the fracture/fragmentation results and a brief comparison with experiment. A second goal in this study is to develop an MD approach that is readily extendible to include the effects of microstructure (e.g., grain size, second phase particle distribution, porosity, microcracks) on the fracture of impact loaded, brittle materials. The application of the model, developed herein, to microstructural effects will be the subject of a future publication.

2. Method

The simulation technique employed in this investigation is based upon the classical molecular dynamics (MD) method, which has been used in the study of atomic level phenomena for over thirty years. In most applications of the MD method, the trajectories of individual atoms are determined by integrating Newton's equation of motion forward in time. Since this approach is based upon individual atoms, it is impractical to apply this method to cases where the important length scales are more than a hundred atom diameters. The focus of the present study is the fracture of impact-loaded solids and the effects of microstructure on fracture. In this case, the important length scales are that of the microstructure and impulse loading (the product of the sound velocity and the duration of loading). Since a typical individual microstructural element may have a length scale of the order of tens of microns, a statistically meaningful ensemble of such elements may, therefore, correspond to a length scale of millimetres. In a face-centred cubic solid with a lattice parameter of 0.34 nm, one cubic millimetre ($\sim$ 100 microstructural length scales) contains 10^{20} atoms which is many orders of magnitude too large to be treated with currently available computers (large MD calculations can account for 10^6–10^8 atoms). MD on an atomic scale must therefore be ruled out for microstructural studies.

Instead of tracing the trajectories of individual atoms, we follow the trajectories of finite size regions of the solid, each consisting of many atoms. Keeping with the usual language of MD, we refer to these individual, many atom regions of the solid as 'particles'. The size of each of these particles is chosen based upon the size of the microstructural features of interest. For example, a simulation of a polycrystalline solid has a natural scale length equal to the grain size. In this case, the particle size should be chosen to be smaller than the size of an individual grain. The lower limit on the particle size is set by the detail that must be resolved within an individual grain. A reasonable choice of particle size, in this case, would be one tenth of a grain diameter. Clearly, in other types of microstructures, appropriate sizes may be easily determined. This point will be discussed at length in a subsequent publication, where we will focus on microstructural issues.

In MD simulations, the trajectories of the individual particles are determined by integrating Newton's equation of motion for each particle forward in time

$$m_i \ddot{r}_i = F_i \tag{1}$$

where m_i, r_i and F_i are the mass of, position of and force on particle i and the double dots indicate two derivatives with respect to time. The force on each particle is determined by its interactions with nearby particles and/or an external loading mechanism, as described below. Several methods have been employed to integrate the equations of motion in MD simulations. In the present study, we have employed the Nordsiek method for integrating equation (1), which is described in detail in [13].

In order to simulate an elastic body, a pair-wise particle interaction energy or potential $\Phi(r_{ij})$ is defined. Φ should be quadratic (harmonic) near its minimum such that linear elasticity is valid for small displacements away from unperturbed equilibrium and it should be very large at small particle separation such that the material becomes very stiff when the compression is large. Many forms of the interparticle energy satisfy these requirements. We choose to employ a relatively simple form of $\Phi(r_{ij})$ which has been used in very many, previous MD simulations and is well-understood: namely, the Lennard-Jones potential

$$\Phi(r_{ij}) = A\left(\frac{r_0}{r_{ij}}\right)^{12} - B\left(\frac{r_0}{r_{ij}}\right)^{6} + C \tag{2}$$

where A, B and C are constants. While this potential was originally constructed to model the interaction between ideal gas atoms, it has since become the *de facto* potential for MD simulations for which physical phenomena, rather than particular atom types, are the focus. This potential is quadratic at its minimum $r_0 = 2^{1/6}(A/B)$ and its slope $(\partial\Phi/\partial r_{ij})$ increases rapidly for $r_{ij} \ll r_0$, where r_{ij} is the separation between particles i and j. This potential is illustrated in figure 1. The constant C is arbitrary, but has been chosen such that the minimum energy $\Phi(r_0)$ equals zero.

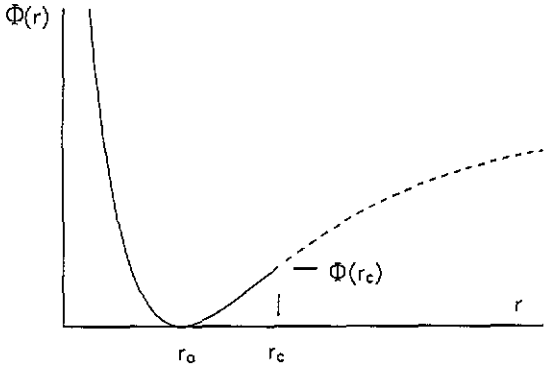

Figure 1. Interparticle pair potential used in the simulations. The potential $\Phi(r)$ is a truncated Lennard-Jones potential. For $r > r_0$, the potential is zero if the bond is broken. A bond is irreversibly broken if the bond energy exceeds $\Phi(r_c)$ in tension.

In the current work, the solid has been discretized as a two-dimensional triangular lattice, which is equivalent to the (111) plane of a face-centred cubic crystal or an (0001) plane in a hexagonal crystal. This lattice was chosen because it is elastically isotropic (with a Poisson ratio of 1/3) and is stable at zero pressure for pair-wise potentials. The elastic constants for this model are summarized in [14] and elsewhere. It should be noted that a two-dimensional lattice of this type does not correspond exactly with either of the classic two-dimensional idealizations of a three-dimensional solid, plane strain or plane stress. The orientation of the lattice is shown in figure 2. Most of the simulations were performed on lattices consisting of 100 particles in the X direction and 101 particles in the Y direction. Additional runs were performed on a 50×201 lattice.

The potential parameters A and B in equation (2) and the particle mass m in equation (1) were chosen to reproduce the properties of the material of interest and the equilibrium particle separation was set by the material density and the number of particles included in the simulation. We arbitrarily set the size of the simulation cell to 1 mm^2. This implies $r_0 = 10^{-5}$ m $= 10$ μm. The interparticle potential parameters were selected to reproduce the properties of Al_2O_3 with an equilibrium particle separation at r_0. The particle mass, m, was determined from the density of Al_2O_3, where we have assumed that the thickness of the simulation cell (i.e., in the z-direction) is equal to r_0. The time step τ used in the integration of the equation of motion was chosen to be a small fraction of the natural vibrational frequency of the solid $[m/(\partial^2\Phi/\partial r^2)]^{1/2}$, such that the violation of energy conservation due to numerical integration remains very low over the course of an entire simulation. All of the relevant parameters defining the interparticle potential and the MD simulations are presented in table 1. The speed of sound in Al_2O_3 is approximately 1.3×10^4 m s^{-1} or $0.15\ r_0/\tau$.

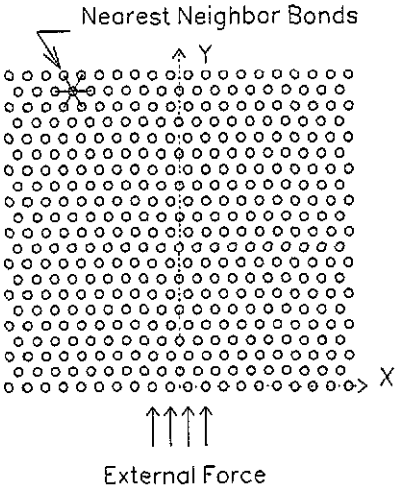

Figure 2. Schematic illustration of the triangular lattice and coordinate system used in the present simulations. Arrows indicate surface particles subjected to the dynamical loading/external force.

Table 1. Data for Al_2O_3 and parametrization of Φ.

Parameter	Value
Density	3.8×10^3 kg m^{-2}
Bulk modulus	350 GPa
Surface energy	4J m^{-2}
r_0	1.0×10^{-5} m
r_c	$1.002r_0$
A	$5.613\,127 \times 10^{-6}$ J
B	$11.226\,25 \times 10^{-6}$ J
C	$5.613\,127 \times 10^{-6}$ J
m	3.2418×10^{-12} kg
τ	1.0×10^{-10} s

The present study focuses on dynamical fracture/fragmentation of impact-loaded solids. While it has been shown [10–12] that fragmentation can be observed in atomistic MD simulations of impact-loaded solids, this fracture is usually caused by localized melting or thermal fluctuations. On the other hand, the fracture and fragmentation of solids is typically associated with the formation and growth of cracks. Except in very unusual cases, crack growth is not reversible. This is because when a crack grows, the atoms at the newly created free surfaces react very quickly with other elements in the environment and because the irregular nature of the crack face prevents full crack closure on removal of the external load. While the energy of the system may be reduced by rebonding the faces of the crack (in the absence of an external loading), the activation barrier for doing so is sufficiently great that complete rebonding is not feasible on time scales of interest. Therefore, the classical MD method must be modified to properly account for the macroscopically irreversible fracture process.

The MD method was modified to account for the macroscopically irreversible nature of the fracture process by assuming that a bond between two particles breaks irreversibly if it is stretched beyond a critical length. This critical length, r_c, at which the bond is considered to

have been stretched beyond its elastic limit and snapped, was selected such that the energy $\Phi(r_c)$, which is liberated from the system when the bond breaks, is equal to the energy required to create a surface of extent equal to that of one particle—i.e., the surface energy per unit area γ divided by the areal particle density on the surface of the host material. This is equivalent to a Griffith criterion for crack propagation, where the critical strain energy release rate G_c is equated with twice the surface energy. In other words, we choose r_c such that $\Phi(r_c) = 2\gamma$. When a bond snaps, the attractive part of the interparticle potential (see figure 1) is removed such that the broken bond interparticle potential Φ_B becomes

$$\Phi_B(r_{ij}) = \begin{cases} \Phi(r_{ij}) & r_{ij} \leqslant r_0 \\ 0 & r_{ij} > r_0 \end{cases} \tag{3}$$

The repulsive part of the broken bond potential is retained such that two particles cannot pass through each other or two opposing crack faces cannot cross when the material is in compression. Particles which are not initially nearest neighbours in the triangular lattice are assumed to interact with the broken bond interparticle potential at all times. It should be noted that with the exception of the energy jump at r_c, the potential and its derivatives are continuous functions of r. While the jump discontinuity at r_c might be unphysical in an atomistic simulation, it is appropriate here and represents the instantaneous snapping of a stretched spring or, equivalently, the dynamic response (spring-back) of a solid to a localized loss of cohesion along a plane or line (i.e., crack propagation). A static version of this simulation procedure was previously applied to the fracture of polycrystalline solids [14–16]. Those studies showed that the simple spring is capable of predicting the intergranular/transgranular fracture morphology [14] with increasing grain boundary toughness in agreement with continuum elasticity calculations, incorporating complex microstructures [15] and qualitatively reproducing many of the observed features of anisotropic thermal expansion induced cracking in non-cubic, polycrystalline ceramics [16].

The simulations were initiated by introducing a time-dependent force on one of the surfaces of the sample. This simulates a dynamic loading of the sample, similar to that which a sample may be subjected to upon impact with a projectile. In this work, external forces were applied in the positive Y-direction to the 10 particles in the center of the $Y = 0$ surface (see figure 2). Additional studies were performed in which the external forces were applied to all of the particles initially on the $Y = 0$ surface. The external force on all other surfaces and particles is always zero. In order to model a hypothetical dynamical loading of the sample, the force was assumed to increase linearly from $F_{ext} = 0$ to F_{max} over a period of $t = 250\tau$ and then decrease to zero during the subsequent 250 time steps. The two-dimensional nature of this model makes representation of point loading or particle impact, in the three-dimensional sense, impossible. In the present simulations, a loading applied over a finite region of the surface is more like the impact of a long bar on the surface rather than a particle impact. As a consequence, the cone-like fracture often observed in particle impact cannot be realistically reproduced, however its two-dimensional analog (cracking in a V-shaped pattern) does occur, as shown below.

The vibrational energy of the system is zero (corresponding to $T = 0$) before the dynamic load is applied, but increases as a result of the energy imparted by the external loading mechanism. Apart from the loading mechanism and the fracture process, this system is adiabatic.

3. Results

During the present dynamic loading simulations, the total energy, number of broken bonds and location of broken bonds were monitored as a function of time. Several different loading amplitudes, two model sizes (100×101 and 50×201) and both localized (10 particles) and uniform (entire $Y = 0$ surface) loadings were examined, as summarized in table 2.

Table 2. Matrix of simulations performed.

F_{max} (N/particle)			
100×101 particle sample		50×201 particle sample	
Narrow impact	Wide impact	Narrow impact	Wide impact
0.2500	0.0750[a]	0.2500	0.0750[a]
0.3125	0.1000	0.3125	0.1000
0.3750	0.1500	0.3750	0.1500
0.5000	0.2500	0.5000	0.2500
0.6250		0.6250	
0.7500			

[a] No bond breaking was observed for these cases.

An example of crack propagation during an impact-loading simulation is shown in figure 3 for the case of dynamic loading over a narrow (10 r_0), central section of the surface where $F_{max} = 0.375N$/particle. The first two frames show that the crack begins in a small central region eight lattice spacings ahead of the center of the impact zone and quickly bifurcates into a small X-shaped crack pattern. The crack radiates forward into the material and backward towards the free surface, where the impact occurred. By the third frame (figure 3(c)), two new, independent cracks have nucleated on either side of the X-crack and begin to grow parallel to the branches of this original X-crack. The direction of propagation of the main X-cracks then begins to shift towards the vertical (i.e., impact direction) and, then, additional crack branching occurs (see figure 3(d)). At late times, new cracks begin to form near the top corners of the sample and grow towards the main cracks (see figures 3(e) and (f)).

Figure 4 shows the evolution of the number of broken bonds and the total energy during the simulation run depicted in figure 3. The bonds begin to break at $t = 250\tau$ (figure 3(a)), which corresponds to the time where the applied force begins to be reduced. Following this initially high damage rate, the rate of increase of the number of broken bonds slows until $t = 950\tau$, where it suddenly accelerates. This acceleration corresponds to the appearance of the first two independent cracks, outside of the main cracks (see figure 3(c)). Following the nucleation and initial growth of these cracks, the damage rate decreases. This creates a plateau in the number of broken bonds versus time plot, which extends to $t = 2500\tau$. At this time step, the damage rate again increases as additional independent cracks nucleate and begin to grow in the vicinity of the upper corners of the sample (figure 3(e)). Following the initial growth of these corner cracks, the damage accumulation rate slows and a second plateau is formed which extends to the end of the simulation run.

The total energy versus time plot (figure 4(b)) shows a close correspondence with the number of broken bonds versus time plot of figure 4(a). At very early times, the energy rises quadratically with time, due to the quadratic dependence of the elastic energy on strain. The energy continues to rise rapidly until $t \approx 500\tau$, which corresponds to the time at which the external force goes to zero. The energy peaks before the force is removed, because

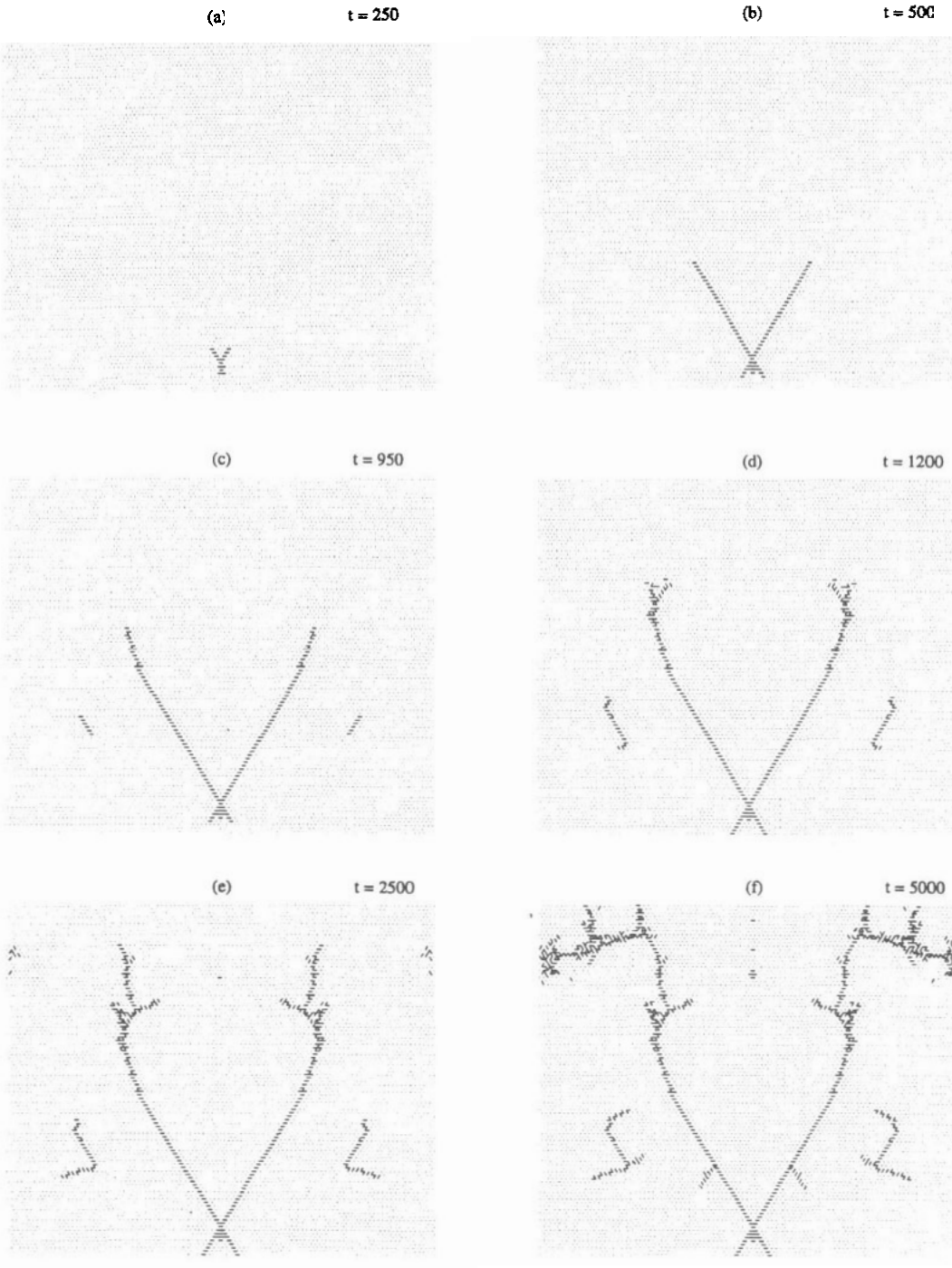

Figure 3. Spatial distribution of broken bonds for the $F_{max} = 0.375N$/particle run of the 100×101 particle sample with narrow impact zone ($10r_0$). Lines drawn between particles in each frame indicate bonds that have been broken on or before the time step in each figure. These figures show the initial particle positions (i.e., the displacements associated with the loading are not shown). Figures (*a*)–(*f*) correspond to times of 250, 500, 950, 1200, 2500 and 5000τ.

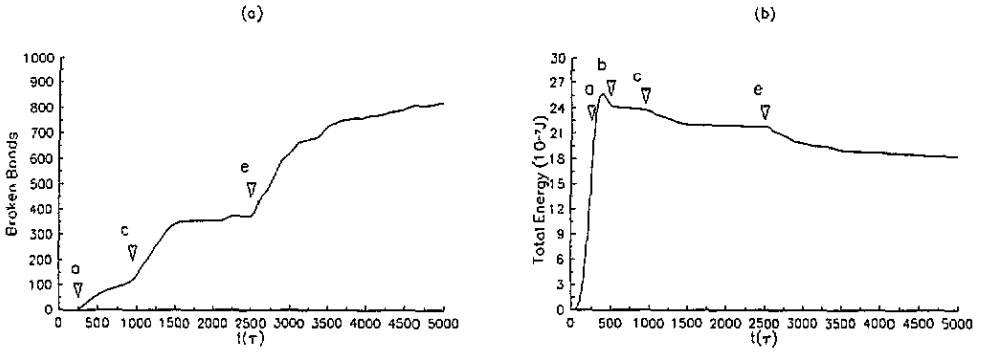

Figure 4. Number of broken bonds (a) and total energy (b) of the 100 × 101 particle sample with narrow impact zone ($10r_0$) for $F_{max} = 0.375N$/particle. The arrows and corresponding labels indicate the times corresponding to the images in figure 3.

of the onset of fracture (at $t \approx 250\tau$), as seen in figures 3 and 4(a). The reduction in system energy, $\Phi(r_c)$, which accompanies each irreversible bond breaking event, causes the total energy to peak before the dynamic loading is removed. For $t > 500\tau$ the total energy continues to decrease as additional bonds are irreversibly broken and no additional energy is supplied by the loading mechanism. This lost energy corresponds to the irreversible process of forming new surface area. The rate of energy decrease accelerates at times corresponding to those in figures 3(c) and (e), where the damage accumulation rate is observed to increase (figure 4(a)). The rate of decay of the energy via bond breaking decreases to nearly zero by the end of the simulation. At this point, the system energy is 1.82×10^{-6} J and is manifested in the form of random vibrational motion of the material particles.

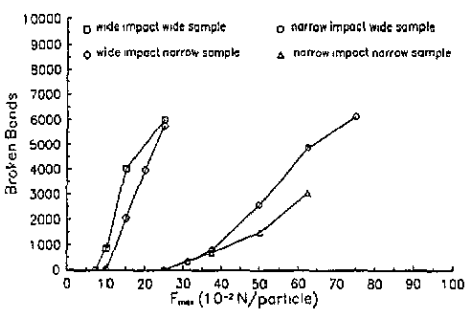

Figure 5. Number of bonds broken at the end of each 5000τ run. Each data point represents one of the simulation conditions indicated in table 2.

The number of broken bonds at the end of each simulation is shown in figure 5 as a function of the strength of the dynamic loading, for both wide and narrow impact zones and wide and narrow samples. For each combination of sample size and loading area, the number of broken bonds increases with increasing loading amplitude (F_{max}). Comparison of the wide impact zone (curves a and b) narrow impact zone (curves c and d) simulations, shows that the threshold loading strength at which bonds begin to break is lower in the wide impact area cases. Additionally, the wide impact area simulations show a larger damage accumulation rate with increasing load strength than do the narrow impact simulations. The

lower damage thresholds, greater damage accumulation rates and total damage accumulated for the wide loading zones is attributable to the fact that the total energy imparted to the sample is proportional to the area under the force-time profile ($500F_{max}\tau$ in the present simulations) *and* the size of the impact zone (number of particles upon which the load is applied).

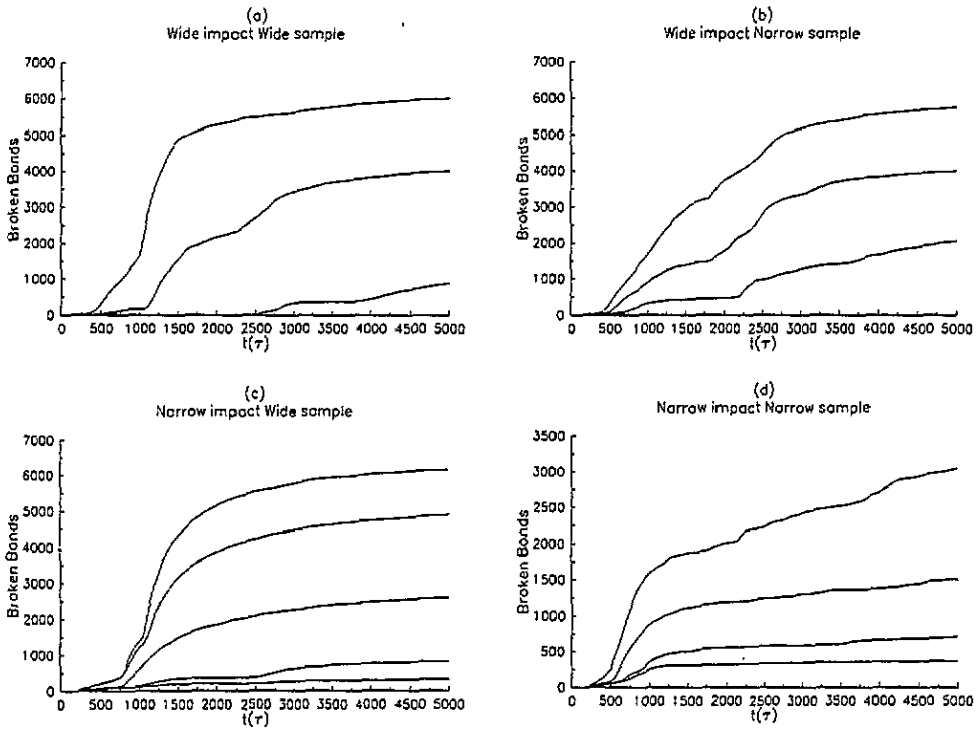

Figure 6. Temporal evolution of the number of broken bonds versus time. (*a*) 100 × 101 particle system with a wide impact zone (entire $Y = 0$ surface). (*b*) 50 × 201 particle system with a wide impact zone (entire $Y = 0$, 50 particle surface). (*c*) 100 × 101 particle system with a narrow impact zone ($10r_0$). (*d*) 50 × 201 particle system with a narrow impact zone ($10r_0$).

The temporal evolution of the damage is shown in figure 6 for all of the loading zone and sample sizes and loading amplitudes (F_{max}) simulated. The basic features of each curve are similar to those shown in figure 4(*a*). The initial rate of damage accumulation is higher when the loading area is larger (cf figures 6(*a*) and (*b*) versus figures 6(*c*) and (*d*)). Damage accumulation occurs more slowly in the long, narrow samples compared with short, wide ones. This is because much of the damage occurs when the compressive wave is reflected off the top surface as a tensile wave. However, the total damage accumulation in the wide loading zone studies is very similar in both wide and narrow samples. On the other hand, the total damage accumulated is considerably lower in the narrow sample than the wide sample when the loading zone is narrow. These observations may be attributed to the fact that the stress wave is much more coherent when the entire surface is uniformly loaded than when only a small loading zone is employed, due to multiple reflections of the stress wave from the sides of the sample in the latter case. In some cases, no bonds are broken until

fairly late times, when the stress waves have been reflected from the free surfaces several times (see figure 6(*a*)).

The spatial distribution of cracks depends sensitively on both the strength of the dynamic loading and the shape of the sample, as is evident from figure 7, where the spatial distribution of broken bonds is plotted for several simulation conditions all with impact zones of size equal to that of the entire $Y = 0$ surface. Figure 7(*a*) corresponds to a low amplitude loading of a wide sample. In this case, the characteristic X-shaped crack pattern (discussed above) occurs only at late times ($t = 2500\tau$) and much farther into the material than found with stronger loading and a narrow impact area (cf figure 3). This X-crack has a different origin than in the narrow loading zone case, where the center of the X is correlated with the size of the loading zone (see below). After the X-crack forms, the pattern of the other cracks formed at late time is also considerably different than that seen in figure 3. When the strength of the dynamic loading is increased (cf figures 7(*a*) and 7(*b*)), the central X-shaped crack is missing and most of the damage starts and occurs near the top of the sample on the left and right sides.

Figures 7(*c*)–(*e*) show the damage accumulation patterns for the long, narrow samples with wide loading zones for different loading strengths. In these runs most of the damage observed in the lower part of the sample is initiated near the start of the simulation and propagates up, into the bulk of the material. The crack bifurcation often seen in the wider samples also occurs here. However, in the low amplitude loading case (figure 7(*c*)), a Y-shaped crack pattern is seen instead of the X-shaped crack pattern. In addition, crack bifurcation occurs many more times in the narrow samples than in the wider/shorter samples (cf figures 7(*a*) and figures 7(*c*)–(*f*)). For all three loading amplitudes, substantial damage occurs both at the lower corners of the sample and in the upper half of the sample. For higher amplitude loading, the region of maximum damage in the upper section of the sample shifts to a position closer to the sample surface opposite the dynamically loaded surface. The damage concentrated near the top of the samples corresponds to the accelerations in breakage rate observed near $t = 2000\tau$ in figure 6(*b*). In each case, the accelerated rate of damage accumulation begins only after the leading edge of the stress wave has been reflected from the top edge of the sample. The X-shaped cracks seen at the higher loading amplitudes (figures 7(*d*) and (*e*)) can be traced back to the corners of the sample, which also are the edges of the loading zone (as in the narrow impact case), as discussed below.

4. Discussion

Examination of the final damaged samples shows the presence of several common features. These include the formation and growth of an X-shaped crack pattern, formation of independent damage regions near the X-shaped crack pattern and near the corners of the sample. It is possible, in many cases, to associate different regions of damage with the initial wave or with reflected waves.

A common feature of the narrow loading zone simulations is that the first bond breaks a finite distance into the solid, ahead of the center of the loading zone. The X-shaped crack pattern grows out from this initial broken bond, which forms the center of the X. The central X-shaped cracks are formed principally from broken horizontal bonds (i.e., bonds that lie in the X-direction), leaving the adjacent bonds (those at 60° to the X-axis) unbroken. (This is an artifact of models which include no bond bending-3 body-terms.) The $+Y$ loading of the $Y = 0$ surface puts the 60° bonds above the edges of the loaded particles into compression, as indicated in figure 8. Therefore, the particles above the edges of the loading zone have

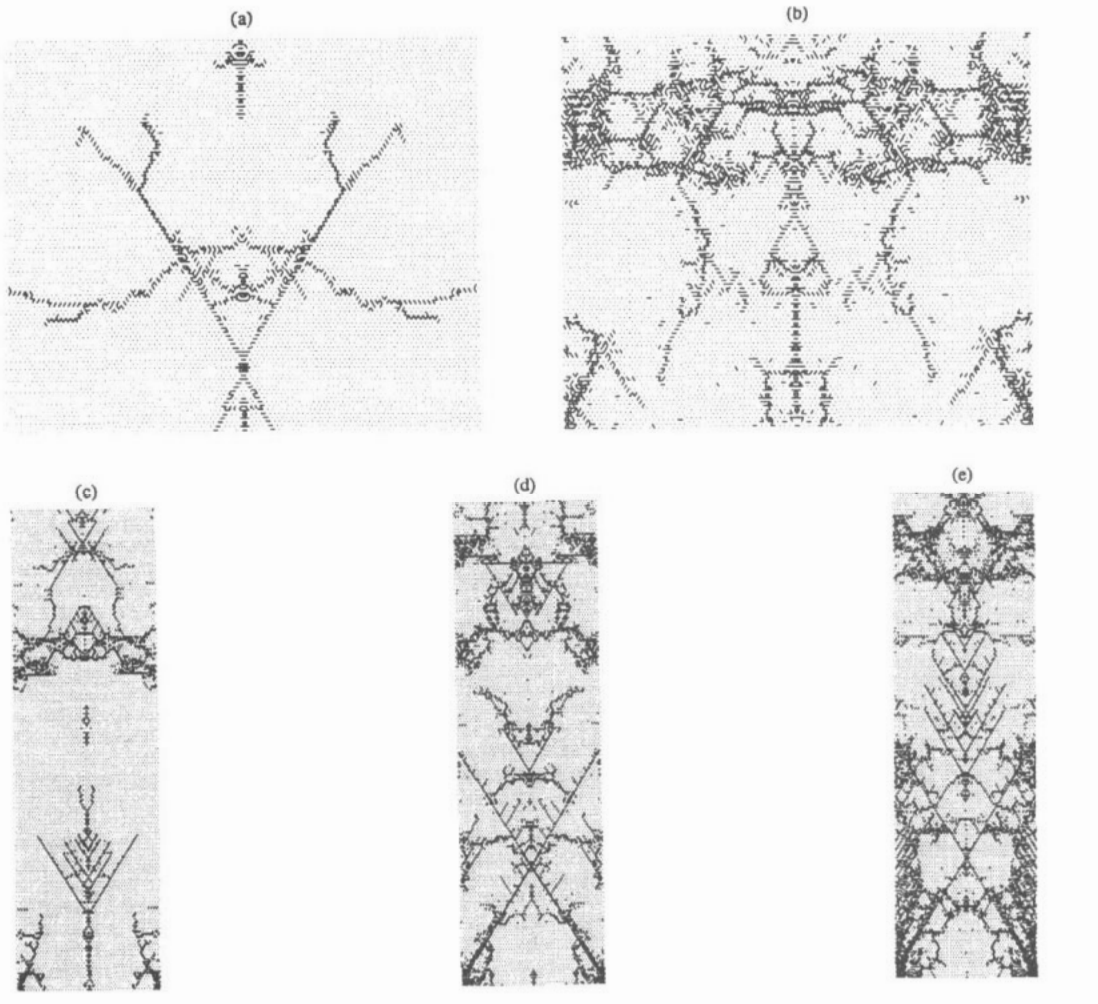

Figure 7. Spatial distributions of broken bonds at the end of the simulations ($t = 5000\tau$) for simulations with wide impact zones (i.e., entire $Y = 0$ surfaces). (*a*) 100×101 particle system with $F_{max} = 0.1N$/particle. (*b*) 100×101 particle system with $F_{max} = 0.15N$/particle. (*c*) 50×201 particle system with $F_{max} = 0.15N$/particle. (*d*) 50×201 particle system with $F_{max} = 0.20N$/particle. (*e*) 50×201 particle system with $F_{max} = 0.25N$/particle.

a component of velocity away from the center of the loaded region. This, in turn, results in a tensile stress in the plane parallel to and above the loading zone. The maximum tensile loading occurs directly above the center of the loaded region. As a result, this is where the first bonds break.

These conclusions can be made more rigorously by appealing to linear elastic continuum theory. In particular, we consider the static version of the narrow loading zone geometry: i.e., the case of a constant, time-independent normal force applied to the free surface ($y = 0$) over a narrow region $-a \leqslant x \leqslant a$. The stress field associated with such a loading was first derived by Michell [17] and may be written as [18]

$$\frac{\sigma_{xx}}{P} = \frac{(\theta_1 - \theta_2)}{\pi} + \frac{2ay}{r_1 r_2}\cos(\theta_1 + \theta_2) \tag{4a}$$

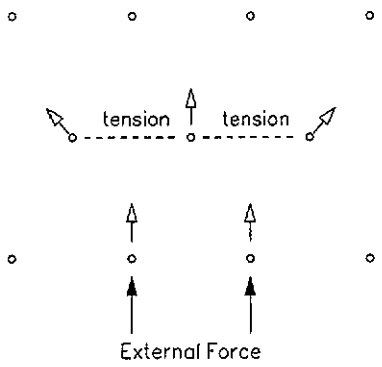

Figure 8. Schematic illustration of the forces and particle relaxations leading to the formation of X-shaped cracks.

$$\frac{\sigma_{yy}}{P} = \frac{(\theta_1 - \theta_2)}{\pi} - \frac{2ay}{r_1 r_2}\cos(\theta_1 + \theta_2) \tag{4b}$$

where $\theta_1 = \tan^{-1}[y/(x-a)]$, $\theta_2 = \tan^{-1}[y/(x+a)]$, $(0 \leqslant \theta_1, \theta_2 \leqslant \pi) r_1^2 = (x-a)^2 + y^2$ and $r_2^2 = (x+a)^2 + y^2$. The maximum tensile stress is σ_{xx} at $x = 0$, at a distance from the bottom (loaded) plane given by $y/a = [(\pi+1)/(\pi-1)]^{1/2} \simeq 1.39$. If we associate a with the half width of the impact zone ($a = 5r_0$), the maximum tensile stress should occur at $x = 0$, $y = 6.95r_0$. Figure 3 shows that the center of the X-shaped crack occurs eight layers from the surface where the impact load is applied, which corresponds to $y = 8r_0 \sin(\pi/3) \approx 6.93r_0$. The close agreement between the simulation and static elasticity results clearly demonstrates that the maximum tensile stress is horizontal and occurs at a height above the center of the loading zone which is proportional to the loading zone size. It should be noted that the extraordinary agreement between the simulation and the continuum theory is likely fortuitous because the discreteness of the lattice is not accounted for in the continuum theory.

After the first bond breaks, it is no longer possible to construct a simple elastic continuum model for the further evolution of the damage. After the first bond breaking event, the crack quickly splits and follows two paths which are symmetric about the vertical centerline (y-axis). This splitting results from a superposition of the tensile wave travelling along y (and spreading along x) away from the impact zone and a horizontal pulse which is induced as each bond breaks at the crack tip. Figure 9 shows the magnitude of the strains in the horizontal bonds on the layers immediately above (and including) where the first bond breaks. Bond breaking creates a horizontal stress pulse that is communicated to the particle layer above the initial broken bond by the 60° bonds. This shifts the position of the maximum horizontal tensile strain up one layer and horizontally by one bond position. As the crack tip progresses through each layer, it steps one additional position to the outside. Before each subsequent bond breaks, there is sufficient time for the strain field in the vicinity of the crack tip to be significantly influenced by the stress pulse caused by earlier bond breaking. This occurs because the crack velocity is slower than the velocity at which the main stress wave travels (see below).

After the tips of the X-shaped crack propagate a finite distance into the sample, the direction of crack propagation curves inward and becomes less regular. The onset of this curvature is correlated with the passing of the initial stress wave. Since the elastic waves move faster than the crack, the trailing edge of the initial stress wave (release

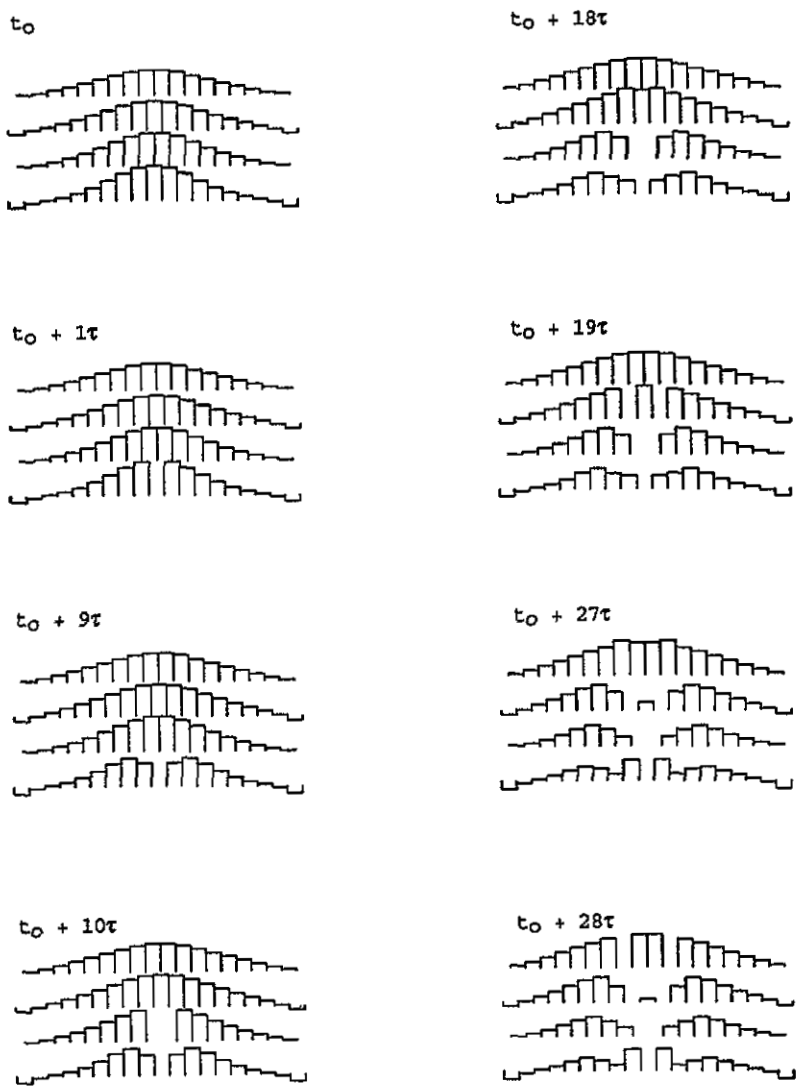

Figure 9. Horizontal displacement of particles on four adjacent, horizontal (parallel to X-axis) layers of particles at several different times. The lowest layer is the one in which a bond breaks first at time $t = t_0$. Successive images show the formation of 2 peaks corresponding to the maximum bond extension and where the next bonds will break. These maxima move away from the $X = 0$ centerline as the stress (strain) wave moves forward in Y.

wave) eventually overtakes the moving crack tip. Once this happens, the strain distribution surrounding the crack tip is significantly altered (most of the compressive strain is relieved) and the mechanism discussed above which had previously kept the crack on a straight diagonal course ceases to operate.

Figure 10 shows the relation between crack propagation velocity and the stress wave velocity for the simulation detailed in figure 3. As shown, when the crack first forms, it travels with a velocity nearly identical to that of the leading edge of the stress wave but then tends to slowly decelerate as it penetrates deeper into the material such that it cannot

quite keep up with the leading edge of the stress wave. At roughly $t = 650\tau$ there is an abrupt deceleration in the crack's velocity. This event occurs as the compressive peak of the stress wave overtakes the crack tip. At earlier times the crack is being pushed ahead of the peak, at later times it is being pulled behind it. Once the transition has occurred, the crack moves significantly slower than the wave front. By $t = 1000\tau$ the trailing edge of the stress wave (i.e., the release wave) has passed the crack tip. It is at this time that the two branches of the X-shaped crack begin to deviate significantly from their original straight (diagonal) course.

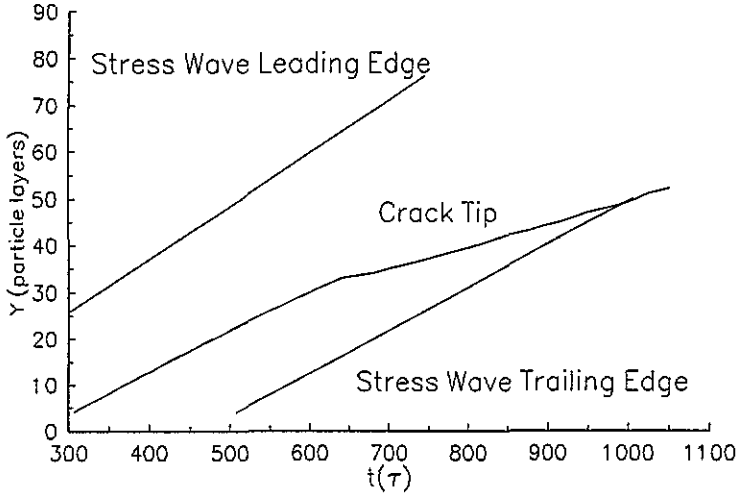

Figure 10. Penetration of the leading and trailing edge of the stress wave and the crack tip for the X-shaped crack of figure 3.

As the stress wave propagates through the solid, the wave form is modified even if no cracking occurs. This too modifies the cracking behavior through the sample and may, in part, also be responsible for a shift in the behavior of the tips of the X-shaped crack. This is demonstrated in figure 11, where we monitor the strains at several distances along a linear chain of particles subjected to the same type of loading used in the present simulations. Although the bonds nearest the surface where the load is applied sustain mainly a compressive strain, subsequent bonds are first put into compression and then tension. The magnitude of the tension caused by the release wave grows as the stress wave propagates deeper into the chain.

Another common feature of virtually all of the simulations is the appearance of cracks which form independently from the X-shaped crack. These independent cracks form at times after the initial stress wave has passed. Therefore, these cracks are likely associated with stress waves which have been reflected from the free surfaces. In order to clarify the role of reflected waves, we have again performed a simulation of a simple linear chain of 20 particles impacted at one end and monitored the strain in the individual bonds (see figure 12). The tensile components of reflected waves can be much larger than the tension associated with the release wave. As a result, the reflected wave is capable of creating damage in the regions that survived the passage of the incident wave.

It is interesting to note that the maximum tensile strain associated with the reflected wave in figure 12 occurs not at the end of the chain, but at a small distance in from the end.

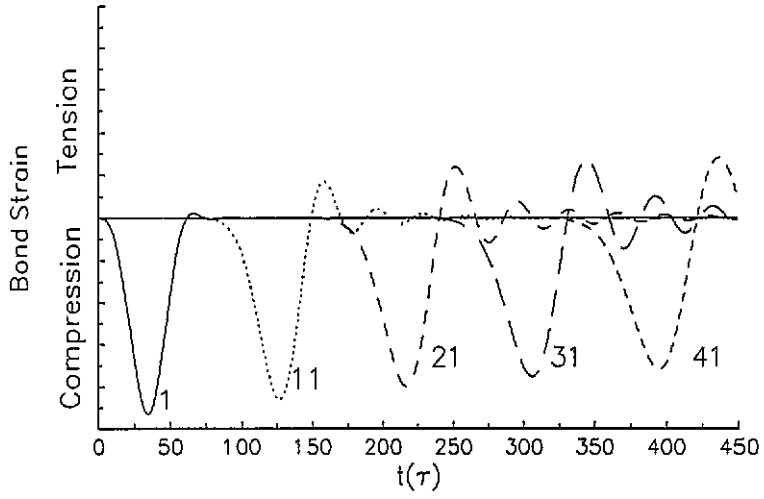

Figure 11. Propagation of a stress wave in a one dimensional chain of 80 particles with a triangular loading profile which reaches a maximum at $t = 25\tau$. Traces show strain versus time for several bonds along the chain, where the surface particle, attached to bond 1, receives the direct dynamical loading.

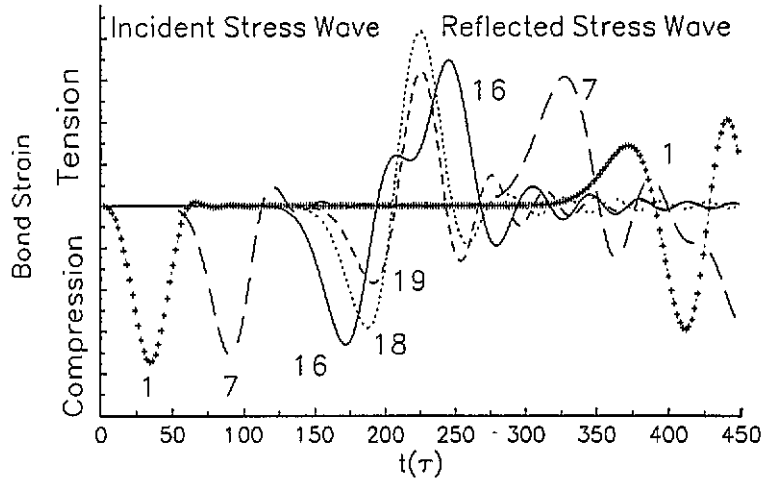

Figure 12. Propagation and reflection of a stress wave in a one dimensional chain of 20 particles with a triangular loading profile which reaches a maximum at $t = 25\tau$. Traces show strain versus time for several bonds along the chain, where the surface particle, attached to bond 1, receives the direct dynamical loading.

This is consistent with the observation that the independent damage regions do not nucleate right at the surface of the 2D samples, but several lattice layers inside the material (see figures 3(*e*) and (*f*) and figures 7(*b*)–(*e*)). Since the incident and reflected stress pulse must cancel each other at the end of the sample, the tensile stress appears where the reflected wave is no longer cancelled by the incident one. Therefore, the tensile stresses should first appear at a distance equal to $c_0 t_0/2$ from the end of the sample, where c_0 is the speed of

sound and t_0 is the duration of the stress pulse [19]. Examination of the high-amplitude impulse data (figures 7(*b*), (*d*), (*e*)), shows that there is a band of damage between 20 and 40 layers from the edge. This corresponds to a stress pulse duration of $t_0 = 230$–460τ, which is consistent with the times of the maximum in and the end of the applied load.

The simulations show several features in common with experimental observation of impact loaded, brittle solids. Both simulations and experiments often show cracks emanating from the edges of a narrow impact zone and converging at a point a finite distance into the sample below the center of the impact zone [19]. Several experimental studies of impact-loaded ceramics [3, 4] have shown that cracking often occurs during the passage of the initial, mainly compressive stress wave, in agreement with our results (see figures 3 and 4). However, the cracking/damage induced by reflected tensile waves is usually greater [4], as also seen in the present simulations. Although this comparison is not exhaustive, it does show that the major features of impact induced damage in brittle materials are reproduced by the present simulation procedure.

As discussed above, one of our main interests in developing this model for impact damage in brittle materials is to investigate the effects of microstructure on damage accumulation. The present model may be easily extended to account for microstructure. The parameters at our disposal for describing microstructural features are the fracture properties (entering through r_c and A and B), the elastic constants (entering through A and B), and the speed of sound (entering through m and A and B) of the different phases in the microstructure. Furthermore, grain boundaries can be modeled as planes of low fracture toughness (r_c) and pre-existing damage by pre-breaking the appropriate density of bonds in the solid. This will be the subject of a subsequent publication [20].

Acknowledgments

This research was supported by the Advanced Research Projects Agency (ARPA) and the Office of Naval Research under Contract N00014-91-J-4019. DJS gratefully acknowledges the hospitality of The Weizmann Institute of Science and the support of the Michael Visiting Professorship.

References

[1] Kunze H D and Meyer L W (ed) 1988 *Proc. Int. Conf. on Impact Loading and Dynamic Behaviour of Materials, IMPACT 87 (DGM, West Germany, 1988)*
[2] Yeshurun Y and Brandon D G 1988 ed H D Kunze and L W Meyer
[3] Pluvinage G and Tolba B 1988 ed H D Kunze and L W Meyer
[4] Louro L H L and Meyers M A 1989 *J. Mater. Sci.* **24** 2516
[5] Holian K S and Burkett M W 1987 *Int. J. Impact. Eng.* **5** 333
[6] Liaw B M, Kobayashi A S, Emery A F and Du J J 1986 *Fracture Mechanics of Ceramics, Volume 7: Composites, Impact, Statistics, and High-Temperature Phenomena* ed R C Bradt, A G Evans, D P H Hasselman and F F Lange (New York: Plenum) pp 187–96
[7] Holian B L 1987 *Phys. Rev.* A **36** 3943
[8] Holian B L, Voter A F, Wagner N H, Ravelo R J, Chen S P, Hoover W G, Hoover C G, Hammerberg J E and Dontje T D 1991 *Phys. Rev.* A **43** 2655
[9] Daw M S and Baskes M I 1984 *Phys. Rev.* B **29** 6443
Foiles S M, Baskes M I and Daw M S 1986 *Phys. Rev.* B **33** 7983
[10] Abraham F F and Rudge W E 1989 *Chem. Phys.* **129** 263
[11] Blink J A and Hoover W G 1985 *Phys. Rev.* A **32** 1027
[12] Holian B L and Grady D E 1988 *Phys. Rev. Lett.* **60** 1355

[13] Beeler J R Jr 1983 *Radiation Effects Computer Experiments* (New York: North-Holland)
[14] Yang W H, Srolovitz D J, Hassold G N and Anderson M P 1990 *Simulation and Theory of Evolving Microstructures* ed M P Anderson and A D Rollett (Warrendale, PA: The Metallurgical Society) pp 277–84
[15] Gibala R, Ghosh A K, Van Aken D C, Srolovitz D J, Basu A, Chang H, Mason D P and Yang W 1992 *Mater. Sci. Eng.* A **155** 147–58
[16] Sridhar N, Yang W H, Srolovitz D J and Fuller E R Jr1994 *J. Amer. Ceram. Soc.* **77** 1123
[17] Michell J H 1902 *Proc. London Math. Soc.* **34** 134
[18] Muskhelishvili N I 1953 *Some Basic Problems of the Mathematical Theory of Elasticity* (Groningen, Holland: Noordhoff) p 389
[19] Cottrell A H 1964 *The Mechanical Properties of Matter* (New York: Wiley) p 166
[20] Smith R W and Srolovitz D J 1994 unpublished